Article

An expansive global oxygenation of Earth's surface environments 1.4 billion years ago

Hao Yan[1], Zheng Qin[2], Lingang Xu [1]✉, Jingwen Mao [3]✉, Dongjie Tang[4], Qin Huang[5], Xiuqing Yang [6], Zhiquan Li[7], Jie Li[8], Long Li [9], Leslie J. Robbins [10], Brian Kendall [11], Donald E. Canfield [12] & Kurt O. Konhauser [9]

The notion of biogeochemical stasis during the Mesoproterozoic era (1.6 to 1.0 billion years ago, Ga) has been increasingly challenged by evidence of transient episodes of increased oxygen (O_2) levels in localized basins. However, the extent of oxygenation during this period - whether local or global - remains a topic of debate. Here, we present evidence of elevated global seawater molybdenum (Mo) isotope values, surpassing the typical Mesoproterozoic baseline, based on manganese (Mn)- and iron (Fe)-rich chemical sedimentary rocks in the ~1.45 Ga Tieling Formation, North China. Mass balance modeling indicates that as much as 80% of the global seafloor was oxygenated. Combined with prior evidence for elevated O_2 levels, our findings suggest a more expanded and prolonged global oxygenation event centered around ~1.4 Ga than previously recognized.

The Mesoproterozoic has traditionally been considered a period of persistently low atmospheric O_2 concentrations, estimated at <0.1% to 1% of present atmospheric levels (PAL)[1–3] (Fig. 1a). Deep oceans were thought to be ferruginous, with oxygenated waters confined to shallow marine settings and euxinic conditions limited to mid-depths along productive continental margins[4–10] (Fig. 1b). However, recent studies have begun to challenge this paradigm, suggesting either that atmospheric O_2 levels may have experienced episodic increases or that baseline O_2 levels were substantially higher - ranging from 2% and 24% PAL - throughout the Mesoproterozoic[11–13] (Fig. 1a). Despite these emerging perspectives, the spatial and temporal dynamics of oceanic oxygenation during this interval remain poorly understood. Although local redox proxies have revealed occasional deepening of the redoxcline within Mesoproterozoic basins[14], such episodes may reflect

localized O_2 production by oxygenic photoautotrophs[15] rather than global shifts in redox state, especially given pronounced ocean redox heterogeneity and atmospheric-oceanic O_2 disequilibrium inferred for this time[16]. Assessing the extent and timing of global ocean oxygenation beyond the confines of individual basins thus requires a more integrated approach.

The interval around ~1.40 Ga is particularly significant because it coincides with the breakup of the supercontinent Nuna (1.45–1.38 Ga)[17] and with a surge in large igneous province (LIP) activity on the continents[18] (Fig. 1c). Large igneous province activity peaked at ~1.38 Ga, with a smaller, earlier pulse around ~1.42 Ga. These events likely had significant impacts on ocean-atmosphere chemistry, continental weathering rates, nutrient delivery, and ocean redox conditions. Evidence for a transient shift towards more oxygenated deep-ocean

[1]School of Earth Sciences and Resources, China University of Geosciences, Beijing, China. [2]Institute of Earth Sciences, China University of Geosciences, Beijing, China. [3]MNR Key Laboratory of Metallogeny and Mineral Assessment, Institute of Mineral Resources, Chinese Academy of Geological Sciences, Beijing, China. [4]State Key Laboratory of Geomicrobiology and Environmental Changes, Frontiers Science Center for Deep-time Digital Earth, China University of Geosciences, Beijing, China. [5]Coral Reef Research Center of China, Guangxi University, Nanning, Guangxi, China. [6]School of Earth Science and Recourses, Chang'an University, Xi'an, Shaanxi, China. [7]Department of Geology, Lakehead University, Lakehead University, Thunder Bay, ON, Canada. [8]State Key Laboratory of Isotope Geochemistry, Guangzhou Institute of Geochemistry, Chinese Academy of Sciences, Guangzhou, Guangdong, China. [9]Department of Earth & Atmospheric Sciences, University of Alberta, Edmonton, AB, Canada. [10]Department of Earth Sciences, University of Regina, Regina, Saskatchewan, Canada. [11]Department of Earth and Environmental Sciences, University of Waterloo, Waterloo, ON, Canada. [12]Nordcee, Department of Biology, University of Southern Denmark, Campusvej 55, Odense, Denmark. ✉e-mail: xulingang@cugb.edu.cn; jingwenmao@263.net
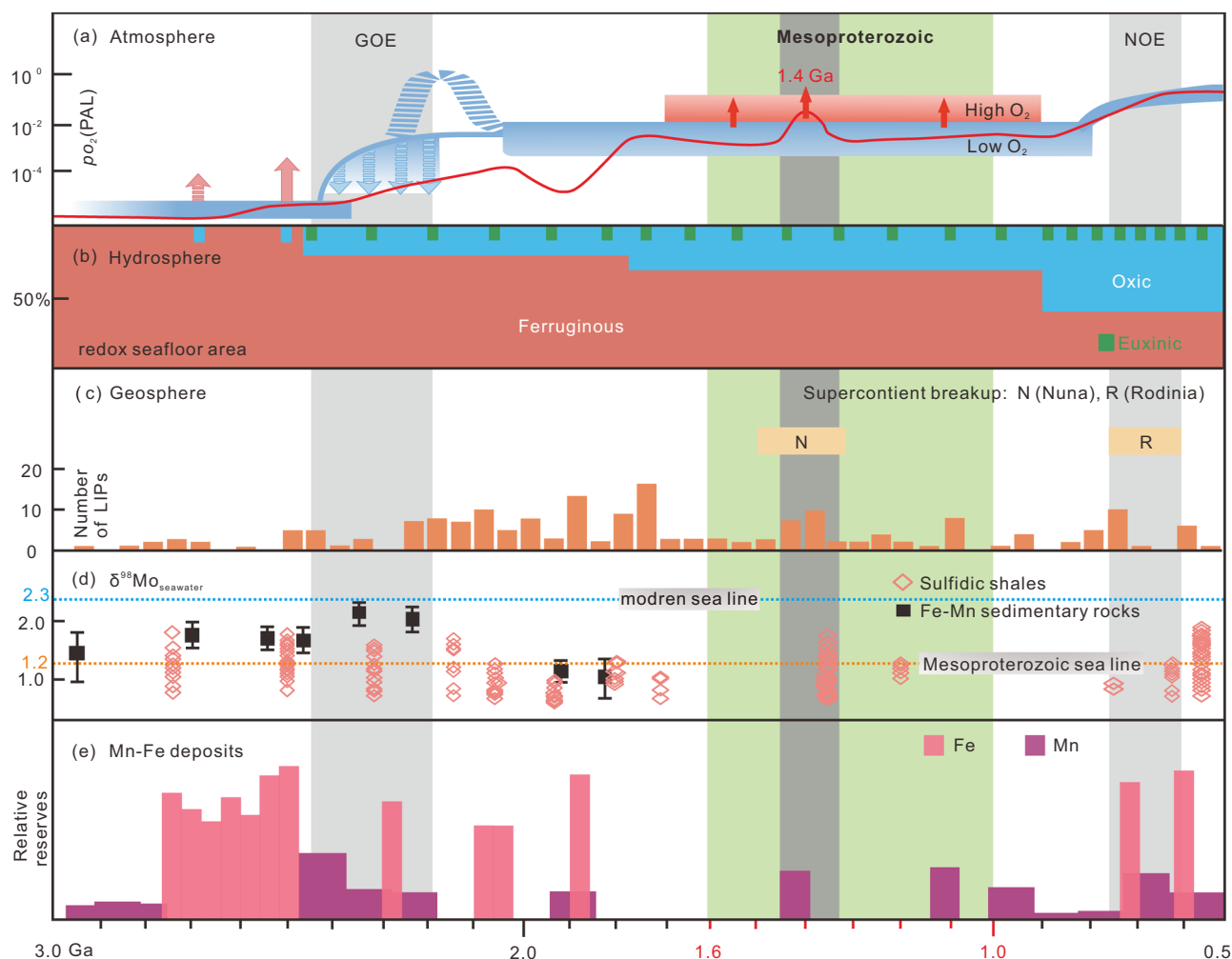
Fig. 1 | Co-evolution of the Earth system during the Precambrian Eon.
a Evolution of atmospheric O_2 levels relative to present atmospheric levels (PAL). Historically, the Mesoproterozoic (ca. 1.6–1.0 Ga, green shading) is characterized by low atmospheric O_2 levels but exceeding that of the Archean[1]. However, several intervals of substantially elevated atmospheric O_2 have been proposed[11,12]. Further, a machine learning model based on mafic igneous geochemical data[13] (red full line) suggests that there was an oxygenation event around 1.4 Ga. **b** Evolution of the hydrosphere, showing partial oxygenation of the surface ocean persisted throughout the Mesoproterozoic, while deeper waters remained dominantly anoxic[6]. **c** Evolution of the geosphere, including the breakup of the supercontinents (Nuna and Rodinia)[17] and the numbers of continental large igneous provinces (LIPs)[18]. Of note, increased LIP formation occurs at approximately 1.4 Ga. **d** Secular

variations in global seawater $\delta^{98}Mo$ reconstructed from euxinic shale and ancient Mn- and Fe-rich sedimentary rocks[28,35,36] (including data compiled from the literature by the cited studies). Among them, the large black rectangles represent temporally binned means (± 1 standard deviation, 1 SD). Orange and blue dashed lines represent the average seawater $\delta^{98}Mo$ during the Mesoproterozoic[7] (1.2‰) and modern[81] (2.3‰), respectively. Due to the lack of a $\delta^{98}Mo_{seawater}$ database for the Mesoproterozoic, it is not possible to compile a complete curve at this time. **e** Distribution of Precambrian sedimentary manganese and iron ore deposits, compiled by relative reserves, in the context of atmospheric oxygenation[82]. The Mesoproterozoic witnessed multiple episodes of sedimentary Mn precipitation (-1.45 Ga and -1.1 Ga) in North China and Western Australia[37,38], respectively. *GOE* Great Oxidation Event; *NOE* Neoproterozoic Oxidation Event.

conditions between 1.40 and 1.35 Ga has been inferred from greater enrichments of redox-sensitive elements, such as Mo, rhenium (Re), and uranium (U), and their isotopic compositions in black shales such as the Velkerri Formation in North Australia and the Xiamaling Formation in North China[19–23]. Consistent with previous studies, elevated iodine (I) concentrations and negative cerium (Ce) anomalies in shallow-water carbonates from the 1.45 Ga Tieling Formation[24–26] – directly underlying the Xiamaling Formation - suggest the potential for a protracted period of elevated O_2 levels in the shallow ocean, at least regionally, around 1.4 Ga. Such a prolonged episode of oxygenation is particularly noteworthy, as it marks a major redox perturbation within the otherwise persistently ferruginous conditions that characterized the Mesoproterozoic oceans[14]. However, the extent of global seafloor oxygenation during this time remains poorly constrained, largely due to the subduction and loss of most ancient deep seafloor records, as

well as the inherent limitations of many geochemical proxies in reliably reconstructing global redox conditions.

Molybdenum is a redox-sensitive element, and variations in its isotopic composition (i.e., the ratio $\delta^{98/95}Mo$, expressed as $\delta^{98}Mo$) in sedimentary rocks have been extensively utilized to track fluctuations in water column redox state[27–29] (Fig. 1d). In modern oceans, the residence time of Mo is approximately 440 kyr[30], significantly surpassing the mean global ocean mixing time of 1–2 kyr. Although the Mo reservoir in the widely anoxic Proterozoic oceans would have been significantly smaller, it was still likely well-mixed globally[5]. Based on well-constrained Mo isotope fractionation and fluxes associated with modern Mo sources and sinks, Mo isotopes are considered a robust proxy for inferring ancient global marine redox conditions[27,31,32]. The global oceanic $\delta^{98}Mo$ value of seawater is primarily governed by the relative burial of Mo under different redox conditions. Strongly euxinic

black shales are particularly valuable for capturing this signal, as Mo is removed nearly quantitatively under high aqueous sulfide concentrations ([H_2S]$_{aq}$ > 11 μM)[33], resulting in minimal isotopic fractionation. In contrast, sediments deposited under all other redox regimes typically exhibit δ^{98}Mo values lower than those of contemporaneous seawater. However, the scarcity of confirmed strongly euxinic shale deposits from the Mesoproterozoic Era has led to significant temporal gaps in the δ^{98}Mo record, limiting our ability to trace global redox evolution during this interval. To address this, we turn to Mn(III/IV) and Fe(III) oxides−hereafter referred to as Mn-oxides and Fe-oxides−which are capable of adsorbing seawater Mo with distinct isotopic fractionations and adsorption efficiencies[34–36]. These metal-rich chemical sediments thus offer a promising alternative archive for reconstructing early Mesoproterozoic seawater δ^{98}Mo and the global extent of ocean oxygenation (Fig. 1d).

In this study, we present Mo isotopic data from two correlative profiles in the northeast of the Yanliao Basin in the North China Craton (NCC), both part of the Tieling Formation at approximately 1.45 Ga. These include (Mn, Fe)-rich sedimentary rocks (economical ore deposit)[37,38] (Fig. 1e) and a suite of regionally stratigraphically equivalent siliciclastic rocks interlayered with dolostone, representing deeper subtidal depositional environments. To elucidate redox conditions in the basin water column, we integrate multiple geochemical proxies: redox-sensitive trace element (RSTE) concentrations, total organic carbon (TOC) contents, Fe speciation data, Fe and Mo isotopes in the siliciclastic rocks, and iodine-to-calcium plus magnesium ratios I/(Ca+Mg) in the dolostones. The δ^{98}Mo values from the (Mn, Fe)-rich sedimentary rocks are then incorporated into a Mo isotope mass balance model to quantitatively estimate the extent of global seafloor oxygenation at the time of deposition. Finally, we re-evaluate the duration and spatial extent of global ocean oxygenation during the 1.45–1.35 Ga interval.

Results and Discussion
Geological setting and samples
The 1.45 Ga Tieling Formation[39], located along the northeastern margin of the Yanliao Basin in the NCC (Fig. S1a–d), is believed to have been deposited in a marine environment connected to the open ocean to the north[40]. This interval coincides with the breakup of Nuna, during which the NCC was positioned at low latitudes (-15°N)[17]. The Tieling Formation is commonly divided into two members. The lower Daizhuangzi (DZZ) Member comprises manganiferous dolostones and shales deposited in an intertidal to deep subtidal environment (approximately 0 to 100 m water depth, respectively). The upper Laohuding (LHD) Member consists of limestones and dolostones deposited in intertidal to shallow subtidal settings (approximately 0 to 20 m water depth)[41] (Fig. S1e).

Two stratigraphic profiles in our study area (41.019°N, 120.143°E) span the DZZ Member, and they consist of approximately 90 m of siliciclastic sedimentary rocks interlayered with dolostones (Fig. 2a, and Mn Fe-rich chemical sediments (Fig. 2b). The succession can be sub-divided into four distinct units, listed from base to top: (i) Unit 1, laminated shale; (ii) Unit 2, dolostone; (iii) Unit 3, mostly manganiferous shale, laterally equivalent to coeval (Mn, Fe)-rich sedimentary rocks observed in a stratigraphically equivalent section located 2 km away; and (iv) Unit 4, red mudstone (Fig. 2a, S2). These four units collectively represent deposition in deeper water environments compared to the carbonate-dominated western region of the Yanliao Basin (see detailed description in Supplementary Information). The (Mn, Fe)-rich sedimentary rocks primarily consist of authigenic (Mn, Fe)-oxides, specifically manganite (MnOOH) and hematite (Fe_2O_3), and diagenetic Ca-rhodochrosite [(Mn, Fe)(Ca)CO_3][38] (Figs. 2b, S3). In this study, we collected samples from all four stratigraphic units as well as the (Mn, Fe)-rich sedimentary rocks. Sample details are provided in Supplementary Information.

Basinal redox assessment
Siliciclastic samples from Unit 1 are characterized by elevated Fe$_{HR}$/Fe$_T$ (>0.38), low Fe$_{py}$/Fe$_{HR}$ ratios (~0), high RSTE (Mo, V, U) concentrations, and high enrichment factors for these elements (RSTE$_{EF}$; EF = enrichment factors: X$_{EF}$ = (X/Al)$_{sample}$/(X/Al)$_{PAAS}$, where X and Al are element-X (ppm) and Al (wt.%) content, respectively, and PAAS = Post-Archean Australian Shale) (Fig. 2a and Supplementary Data 1). Collectively, these data suggest deposition under anoxic and ferruginous bottom water conditions during Unit 1. This interpretation of redox conditions is further supported by iron speciation and isotope data. Units 1, 3 and 4 all exhibit Fe$_{OX}$/Fe$_{HR}$ ratios >0.8 (Fig. S4a), indicating that Fe$_{HR}$ is primarily associated with Fe-oxides. The δ^{56}Fe values of authigenic Fe-oxides in sediments reflect the extent of Fe(II) oxidation during deposition[42,43]. In well-oxygenated waters, oxidation of seawater Fe(II) is quantitative, and iron-oxides inherit the δ^{56}Fe values of the Fe(II) source[44]. In contrast, under suboxic to anoxic conditions, partial Fe(II) oxidation results in isotopic fractionation, enriching Fe-oxides in ^{56}Fe by up to +3‰[44,45]. Given that seawater has a relatively homogeneous Fe isotope composition of close to 0‰[44], the positive δ^{56}Fe$_{HR}$ values in Unit 1 samples of between +0.46‰ and +0.78‰ (Fig. 2a; see Methods for details) are best explained by partial oxidation of a deep Fe(II) reservoir under suboxic-anoxic shallow waters at the studied localities. Subsequently, an increase in I/(Ca+Mg) ratios - from ~0 μmol/mol to a peak of ~1.30 μmol/mol in the Unit 2 dolostone - may signal a shift towards more oxygenated bottom waters immediately preceding the deposition of Unit 3 (Fig. 2a; see Supplementary Information for details).

In contrast to Unit 1, siliciclastic samples from Units 3 and 4 have high total Fe and/or Mn concentrations (Fig. 2a). These units also display positive Eu anomalies (Eu/Eu* = 1.1–1.4; Eu/Eu* = Eu$_{PAAS}$/(0.67 × Sm$_{PAAS}$ + 0.33 × Tb$_{PAAS}$) (Fig. 2a), consistent with a hydrothermal influence. The metallogenic characteristics of Unit 3, in particular, suggest hydrothermal vent activity in deeper waters, which likely delivered abundant dissolved Fe(II) and Mn(II) below the redox chemocline, resulting in localized metal enrichment[38]. Under such conditions, extensive Fe precipitation at the redox chemocline may obscure Fe speciation signals, complicating reconstructions of bottom-water redox conditions for Units 3 and 4. Compared to Unit 1, the low RSTE$_{EF}$ and TOC contents in Unit 3 likely indicate the persistence of oxic bottom-water conditions established during the deposition of Unit 2, rather than a return to ferruginous conditions. The input of hydrothermal Fe(II) would also shift the Fe isotopic composition of the local water column towards the hydrothermal endmember (−0.5‰ to 0‰)[44]. Consistent with this, most of the Unit 3 samples show δ^{56}Fe$_{HR}$ values (−0.49‰ to −0.38‰; Fig. 2a) that are similar to those of hydrothermal fluids, supporting the interpretation of quantitative oxidation of hydrothermally derived Fe(II) under oxic conditions - similar to what is observed in contemporary Mn-Fe-rich chemical sediments (−0.45‰ to −0.30‰; Fig. 2b). Notably, several Unit 3 samples show even more negative δ^{56}Fe$_{HR}$ values (−0.71‰, −0.78‰ and −0.99‰; Fig. 2a), indicating an additional source of isotopically light Fe(II), most likely derived from dissimilatory Fe(III) reduction (DIR) of continentally-sourced minerals, which typically yield δ^{56}Fe values between −2.5‰ and −0.5‰[44].

Further evidence for oxic water-column conditions during the deposition of Unit 3 comes from a pronounced negative δ^{98}Mo excursion, dropping from values as high as +0.80‰ in Unit 1 to as low as −0.43‰ in Unit 3. This isotopic shift, coupled with variable Mn and Fe concentrations (Fig. 2a), is consistent with the preferential adsorption of lighter Mo isotopes onto Mn-oxides and Fe-oxides[34]. Among these, Mn-oxides have a particularly strong affinity for light Mo isotopes and induce greater isotopic fractionation than Fe-oxides, such as ferrihydrite[35,46–48]. Accordingly, the strong negative correlation observed between Mn/Fe ratios and δ^{98}Mo values across Units 1 to 3 provides compelling evidence for Mn-oxide precipitation and burial
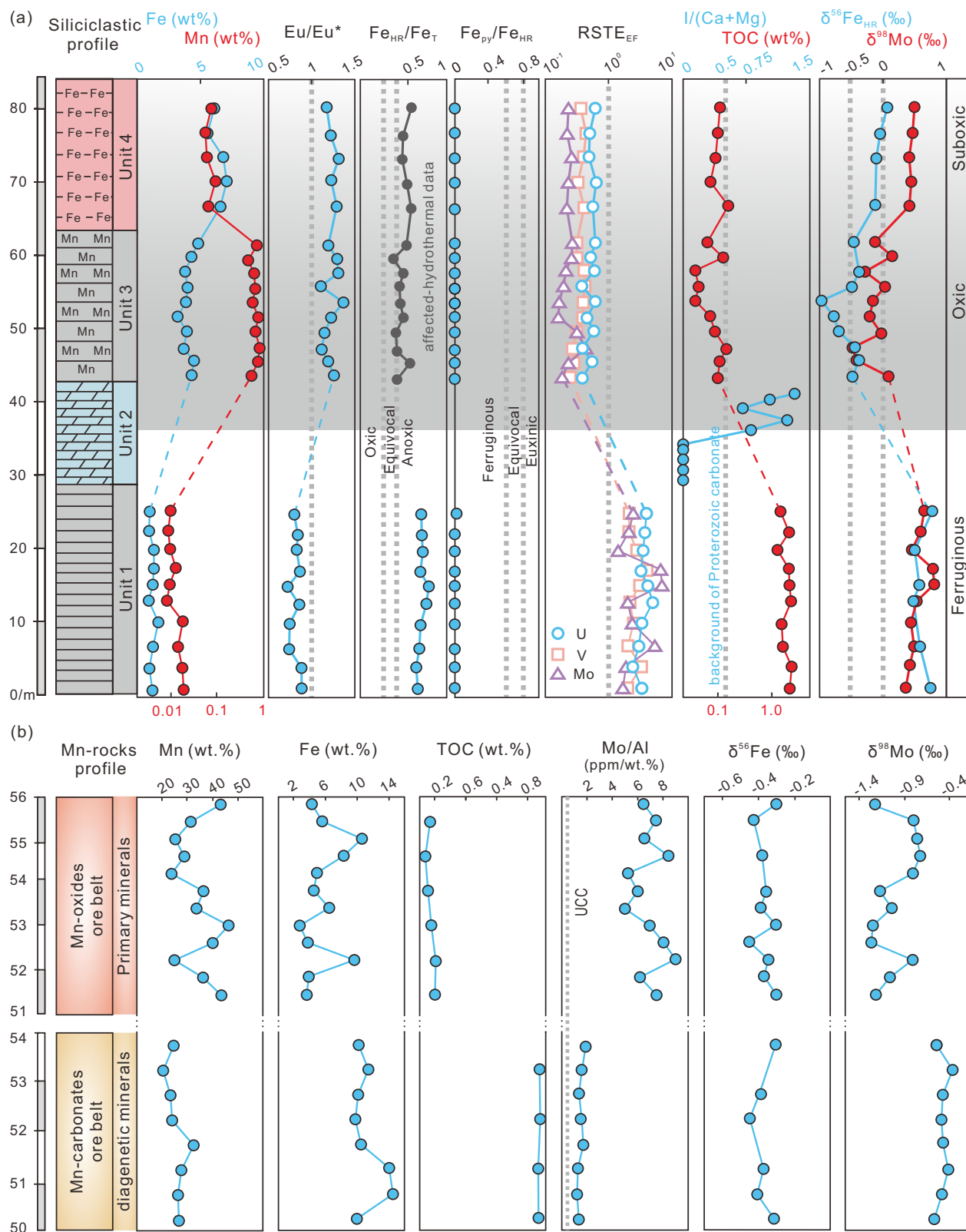
during Unit 3 deposition (Fig. S4b). This implies significant water-column oxygenation and the downward penetration of O₂ below the sediment-water interface[49].

Unit 4 samples show a slight increase in $\delta^{56}Fe_{HR}$ (−0.13‰ to +0.05‰) and are characterized by $RSTE_{EF}$ and TOC contents similar to those of Unit 3, but with lower Mn/Fe ratios and higher $\delta^{98}Mo$ values (Fig. 2a). These geochemical trends suggest that Unit 4 was deposited

under somewhat less oxygenated, possibly suboxic, bottom-water conditions. When considered alongside the evidence for shallow water oxygenation from the carbonate-dominated western regions[24–26], our findings suggest a deepening of the redoxcline and an expansion of water column oxygenation in the basin during deposition of the 1.45 Ga Tieling Formation. This peak in oxygenation appears to be particularly pronounced during the Mn-rich depositional intervals of Unit 3.

Fig. 2 | Geochemical and isotopic profiles. a Dashed lines on Fe_{HR}/Fe_T profiles represent calibrated thresholds indicative of oxic (<0.22) and anoxic (>0.38) water column conditions[9]. Black circles in the Fe_{HR}/Fe_T profiles represent an extra supply of hydrothermal iron that affects interpretation of Fe speciation data (see text for detailed explanation). The dashed lines on the Fe_{py}/Fe_{HR} profiles represent the lower (0.6) and upper (0.8) thresholds for euxinia[9]. Dashed lines on I/(Ca + Mg) profiles represent the baseline (-0.5) for Precambrian carbonates[24]. Shading indicates the approximate position of cycles from ferruginous (white) to oxic (gray) to suboxic (transition color) conditions. **b** Coeval with Unit 3 Mn-rich shale, other Mn-rich sedimentary rocks can be subdivided into two ore belts of primary Mn-oxide and diagenetic Mn-carbonates, respectively[38]. Dashed lines on elemental ratio profiles represent the average upper continental crust (UCC)[50]. The high Mo/Al contents and high Mn-Fe contents exclude the influence of detrital Mo. Oxygenated conditions during deposition of these Mn-rich rocks are verified by uniformly negative $\delta^{98}Mo$ and $\delta^{56}Fe$ values and a decrease in redox-sensitive trace-element (RSTE) enrichment factors. The error bars for $\delta^{98}Mo$ and $\delta^{56}Fe$ are smaller than symbol sizes. *TOC* Total Organic Carbon Content.

To assess whether this oxygenation event reflects a more widespread phenomenon rather than a localized feature of a single continental margin, we further utilize Mo isotope data to evaluate the extent and intensity of deep-water oxygenation at a global scale during this time.

Global seawater Mo isotope composition at ~1.45 Ga

Ferruginous shales from our siliciclastic section cannot reliably constrain the global seawater Mo isotope signature due to multiple isotope fractionation processes arising from Mo removal from seawater via adsorption onto oxides, organic matter, and sulfides[27]. In contrast, (Mn,Fe)-rich chemical sedimentary rocks offer a more robust archive for reconstructing ancient seawater $\delta^{98}Mo$. Their formation under oxygenated bottom-water conditions supports the preservation of primary Mn- and Fe-oxides, as previously demonstrated by Yan et al.[38]. Nonetheless, this inference depends on a well-constrained understanding of both the magnitude of isotope fractionation and the adsorption efficiencies associated with Mo uptake onto Mn- and Fe-oxide precursors[36].

The (Mn,Fe)-rich chemical sedimentary rocks in our study exhibit high Mo/Al ratios (1.2 to 9.0 ppm/wt.%), significantly exceeding the upper continental crust (UCC) average of 0.18[50], along with high Mn (20–42 wt.%) and Fe (up to 14 wt.%) concentrations (Fig. 2b). These characteristics indicate that Mo enrichment was mainly derived from the adsorption onto Mn- and Fe-oxides, rather than from detrital input. Generally, (Mn,Fe)-rich chemical sedimentary rocks with either high (>10^1) or low (<10^{-1}) Mn/Fe ratios display relatively uniform $\delta^{98}Mo$ values, primarily influenced by isotopic fractionation during the adsorption of Mo onto Mn- and Fe-oxides, respectively[35]. In contrast, rocks with intermediate Mn/Fe ratios (10^{-1} to 10^1) have $\delta^{98}Mo$ values that reflect the relative contributions of Mn- and Fe-oxides, displaying an inverse linear correlation between $\delta^{98}Mo$ values and Mn/Fe ratios[35]. The evolutionary trend between Mn/Fe ratios (15.88 to 1.68) and $\delta^{98}Mo$ values (−1.25‰ to −0.35‰) observed in our (Mn, Fe)-rich sedimentary rocks is consistent with this model (Fig. S4c). However, the $\delta^{98}Mo$ values of (Mn, Fe)-carbonate rocks deviate from this trend despite sharing similar Mn/Fe ratios with oxide-rich samples (purple rectangle in Fig. S5). This deviation suggests that certain Mn-Fe-rich sedimentary rocks—particularly those with elevated TOC (Fig. 2b) or those significantly altered during diagenesis—are unsuitable for reconstructing seawater $\delta^{98}Mo$.

The reduction of primary Mn- and Fe-oxides during diagenesis can remobilize previously adsorbed Mo, leading to its release into pore waters and subsequent incorporation into diagenetic carbonates[38]. Non-quantitative Mo scavenging from pore fluids and potential exchange with the overlying water column can result in complex and variable Mo isotope fractionation during carbonate formation[51]. Organic matter also plays a role: Mo adsorption onto organic carbon occurs via a distinct fractionation pathway from that of Mn- and Fe-oxides, introducing additional complexity[36]. As a result, TOC-rich (Mn, Fe) carbonates provide unreliable archives for reconstructing the global seawater Mo isotopic composition.

Given these considerations, we restrict our reconstruction of seawater $\delta^{98}Mo$ to samples composed of primary Mn- and Fe-oxides (e.g., manganite and hematite) that exhibit low TOC contents and minimal evidence of diagenetic alteration[38]. Using these well-preserved samples, we calculate Mo isotope fractionation between seawater and oxide phases to estimate contemporaneous global seawater $\delta^{98}Mo$ values. The results yield a mean value of +1.72 ± 0.13‰ (1 standard deviation, 1 SD) defined as the seawater $\delta^{98}Mo$ signal, with higher seawater values possible if there was any multi-stage Mo isotope fractionation associated with Mn-cycling (see Supplementary Information for details). Our findings, when coupled with previous studies on the Xiamaling Formation in North China - where shales $\delta^{98}Mo$ values reach up to +1.70‰ at ~1.37 Ga[20,21] - indicate that global seawater $\delta^{98}Mo$ around 1.4 Ga was elevated relative to the long-term Mesoproterozoic baseline of +1.20‰[7,28,52–54] (see Supplementary Information for details).

Estimate of global ocean oxygenation at ~1.45 Ga

Our study utilizes steady-state isotopic mass-balance modeling (see Supplementary Information and Figs. S6, S7 for details) to interpret the high seawater $\delta^{98}Mo$ values of at least 1.72‰ at ~1.45 Ga. The models suggest that approximately 80% of the global seafloor area was oxygenated at this time (Fig. 3a). This estimate is comparable to previous reconstructions of widespread oxygenation during the ~1.56 and ~1.36 Ga episodes, as recorded by high seawater $\delta^{98}Mo$ value of 2.03‰ in the Gaoyuzhuang Formation, North China[29], and by U isotopic and Re mass balance models for the Velkerri Formation, Northern Australia[19,23]. Notably, our estimate of 80% oxygenated seafloor surpasses previous estimates of <50% oxygenation for mid-Proterozoic seafloor based on Cr and U concentrations in shales[5,55].

In the anoxic deep oceans of the Mesoproterozoic Era, the dissolved seawater Mn(II) reservoir may have been at least one order of magnitude greater than today[56]. Around ~1.45 Ga, this reservoir was probably further augmented by substantial hydrothermal Mn(II) inputs, as evidenced by the widespread deposition of economic Mn ore deposits across multiple basins at that time[37,38]. The formation and burial of Mn-oxides typically requires at least tens of μM of dissolved O_2 concentrations in bottom waters, along with sufficient O_2 penetration into sediments[49,57]. Since Mn-oxides are a major sink for Mo in oxic environments[27], the extensive seafloor oxygenation predicted by our model implies that bottom-water O_2 concentrations exceeded tens of μM across much of the global deep ocean at ~1.45 Ga. Such widespread deep-ocean oxygenation would have been difficult to achieve through shallow-water oxygenic photosynthesis alone, which likely produced waters with no more than 10 μM O_2[15], especially considering respiratory consumption of O_2 by the biological carbon pump in the ocean interior[16]. Thus, elevated atmospheric O_2 levels must also have been present to ensure sufficient O_2 delivery into the deep ocean. This interpretation is consistent with emerging geochemical evidence, including predictions of high atmospheric O_2 around 1.4 Ga from machine learning analyses of igneous geochemical datasets[13], as well as a range of sedimentary redox proxies[11,12].

Implications for expansive oxygenation at 1.45–1.35 Ga

Previous studies have identified transient episodes of atmospheric and global oceanic oxygenation between 1.40–1.35 Ga that disrupted long-term redox stasis of the Mesoproterozoic[11,19–23]. Positive Cr isotope fractionations in Mesoproterozoic carbonates, which can be traced back to as early as ~1.42 Ga[58], further support the onset of atmospheric
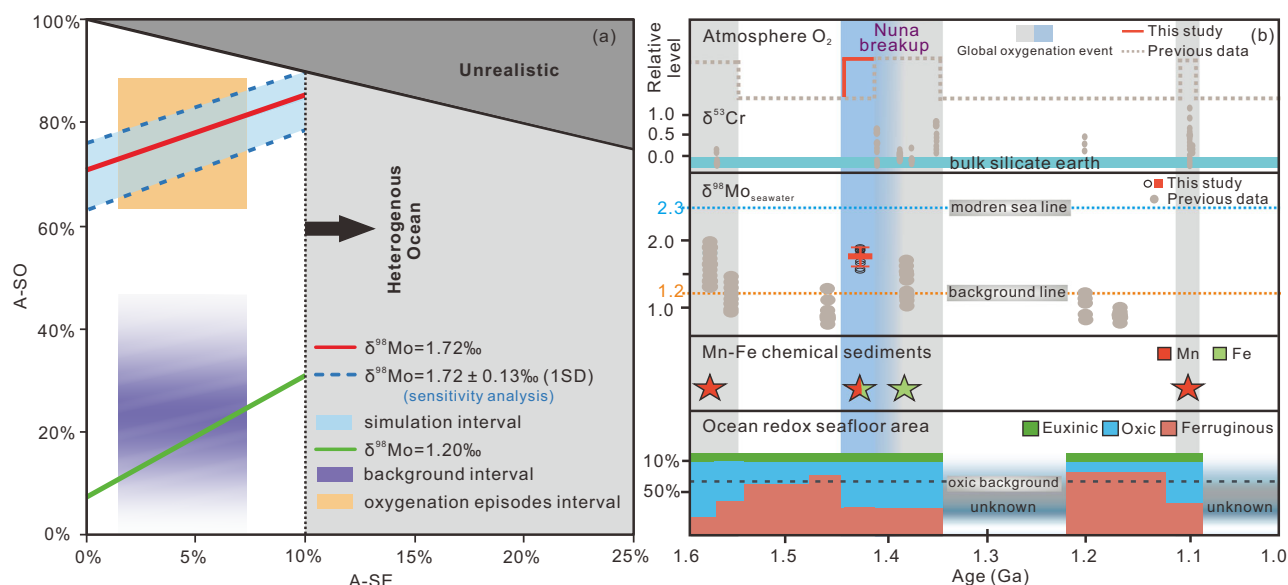
Fig. 3 | Steady-state isotopic mass-balance model and summary of atmosphere and global ocean redox chemistry during the Mesoproterozoic. a Modeling used a seawater $\delta^{98}Mo$ value of 1.72‰ from the mean calculated value derived from Mn- and Fe-oxide data in our study (red full line). The mean value ± 1 standard deviation (SD) are provided to account for the results of a sensitivity analysis (blue dotted line). The green full line represents the simulation result using the background value of the Mesoproterozoic seawater Mo isotope (1.2‰). A Mo isotope fractionation of $-0.65‰^{[28]}$ was used for the intermediate Mo sink in the isotopic mass-balance model (see Supplementary Information for detailed explanation). Our model yields a higher global-ocean oxygenated area than the background Mesoproterozoic interval (purple, areas of high color intensity denote the core density of the data distribution) as modified from [5,55,83], but is comparable to

previous assessments of Mesoproterozoic oxygenation episodes at 1.56 and 1.36 Ga (tan interval)[19,23,29]. The right gray area represents states where the euxinic sinks are dominant, so that the dissolved Mo isotope ratio in the oceans becomes heterogenous. The shaded area in the top right corner represents an unrealistic areal proportion of euxinic and strongly oxic conditions over 100%. A-SO: global oxic seafloor area; A-SE: global euxinic seafloor area. **b** In the $\delta^{98}Mo_{seawater}$ compilation panel, the large pink rectangle represents binned means (± 1 SD). The back-calculated $\delta^{98}Mo$ values by Mn oxide samples are shown as black hollow circles. Compared with a series of Mesoproterozoic oxygenation episodes, our study reveals a prolonged global oxygenation event at ~1.45–1.35 Ga (blue and gray shadings). Data sources: Cr isotopes from [58,84,85]; Mo isotopes from this study and [7,52]; Mn-Fe chemical sediments distribution from [37,38,62,63].

oxygenation during this interval. Our Mo isotope data for ~1.45 Ga offers a crucial snapshot that likely captures the early stages of this expanded oxygenation event. In the broader context of episodic Mesoproterozoic oxygenation, our study identifies a prolonged period (1.45–1.35 Ga) during which anomalously high levels of global ocean–atmosphere O_2 levels were common and potentially even continuous. By contrast, other Mesoproterozoic oxygenation events, notably at ~1.56 Ga and 1.1 Ga, are currently thought to be shorter in duration, and in each case their evidence is limited to a single locality[32] (Fig. 3b).

The prolonged oxygenation event we identify may have been fueled by enhanced primary productivity linked to greater nutrient delivery - particularly phosphorous - from the weathering of LIPs during the breakup of Nuna[59–61]. Simultaneously, the development of rift basins along continental margins facilitated the burial of Mn-Fe chemical sediments, supported by enhanced hydrothermal activity[37,38,62,63] (Fig. 3b). Although LIP-driven weathering and Mn-Fe deposition also characterized the breakup of Rodinia in the Early Neoproterozoic[64], the more limited breakup of Nuna may have resulted in a weaker perturbation of the ocean-atmosphere system[65,66]. This could have constrained the duration and intensity of photosynthetic O_2 production, confining it to a geologically short time interval at 1.45–1.35 Ga. Nevertheless, the increased O_2 availability during this interval may have been sufficient to tip the surface redox balance toward a more O_2-rich atmosphere. This is consistent with the growing prevalence and magnitude of positively fractionated Cr isotope signals during and after ~1.40 Ga[32] (Fig. 3b). This stepwise rise in oxygenation implied by our findings underscores the importance of Mesoproterozoic processes as precursors to the more dramatic oxygenation events of the Neoproterozoic.

Methods

Major and trace element analyses

For major element analysis, sample powders were fluxed with $Li_2B_4O_7$ (1:8) to make homogeneous glass disks at 1250 °C, using a V8C automatic fusion machine (Analymate Company), then analyzed using X-ray fluorescence (Zetium, PANalytical or XRF-1800, Shimadzu) at Yanduzhongshi Geological Analysis Laboratories Ltd. The analytical errors for major elements are estimated to be within 1% based on four replicate analyses of Chinese national standards. For trace element analysis, approximately 50 mg of finely powdered sample was digested with a mixed acid solution containing 1 mL of hydrofluoric acid (HF) and 1 mL nitric acid (HNO₃) at 190 °C for over 48 h in sealed Teflon vessels. After digestion, 1–2 mL of perchloric acid (HClO₄) was added for further dissolution, then dried down and diluted to 100 g with 2% HNO₃ and analyzed for trace elements using an Agilent 7700x inductively coupled plasma mass spectrometer (ICP-MS). Analytical precision, monitored based on replicate measurements of the Chinese reference material GSR-2, was better than 5%.

Organic carbon content (TOC)

For TOC measurements, siliciclastic rocks were leached with excess ~20% hydrochloric acid to remove carbonate phases and washed in distilled water prior to analysis at the State Key Laboratory of Geological Processes and Mineral Resources (GPMR), China University of Geosciences (Wuhan). The dried residue and non-acidified samples were measured using a Jena Multi-EA 4000 carbon-sulfur analyzer. Analytical precision was better than 0.2%, as determined from repeated measurements of the Alpha Resources reference material AR4007 (7.27 wt.% TOC contents).

Iodine-to-calcium+magnesium analyses

For I/(Ca + Mg) analyses of dolomite, sample powders (<200 mesh) were rinsed four times with 18.25 MΩ Milli-Q (MQ) water to remove adsorbed clays and soluble salts. After drying, approximately 5 mg of the cleaned powders were further homogenized in an agate mortar and accurately weighed. The cleaned powders were dissolved in 3% HNO_3 for 40 min and then centrifuged to obtain the supernatant. Determination of Ca and Mg contents was performed on matrix solutions prepared in 3% HNO_3 and diluted 1:50,000, using a Perkin-Elmer NexION 300Q inductively coupled plasma mass spectrometer (ICP-MS) at the National Research Center for Geoanalysis, Beijing. JDo-1 (dolostone reference material) was run as a bracketing standard every nine samples to monitor analytical performance; analytical uncertainties were <3% for Mg and <2% for Ca. For I analysis, 1 mL of the supernatant was diluted in a 0.5% MQ water to stabilize iodine[24], and analyzed within 48 h using a Thermo Fisher Scientific Neptune Plus multi-collector ICP-MS. The rinse solution for each analysis contained 0.5% HNO_3, 0.5% tertiary amine, and 50 μg/g Ca, with a rinse duration of approximately 1 min. Analytical uncertainty for ^{127}I, evaluated from repeated measurements of GSR-12 and duplicate samples, was ≤ 6%, and long-term accuracy was verified by repeated analyses of the GSR-12 reference material[67].

Iron speciation analyses

Iron speciation analyses were performed on siliciclastic rocks containing >0.5 wt.% total Fe at the State Key Laboratory of Biogeology and Environmental Geology, China University of Geosciences, Wuhan. Sequential extraction procedures were carried out to quantify Fe associated with carbonate (Fe_{carb}), magnetite (Fe_{mag}), and ferric oxides (Fe_{ox}), following the method of Poulton & Canfield[68]. Fe_{carb} was extracted with a sodium acetate solution (pH 4.5) at 50 °C for 48 h; Fe_{ox} was targeted using a sodium dithionite solution (pH 4.8) for 2 h at room temperature; and Fe_{mag} was extracted with ammonium oxalate for 6 h at room temperature. Iron concentrations in all extracts were determined by atomic absorption spectrometry, with relative standard deviations (RSDs) of replicate measurements below 5%. Pyrite-associated Fe (Fe_{py}) was determined by gravimetric precipitation of Ag_2S following a standard chromous chloride reduction[69].

Fe isotope analyses

Fe isotope compositions for siliciclastic rocks and Mn-Fe-rich chemical sediments were undertaken by following those suggested by Hou et al.[70] at the Key Laboratory of Mineralization and Resource Assessment of the Ministry of Land and Resources in Beijing. Briefly, samples were dissolved in 3 mL aqua regia, whereas BCR-2 and BIR-1 standards were digested in 2.4 ml HF and 0.6 mL HNO_3 at 140 °C for 72 h. All solutions were converted to a 7 M HCl matrix for further purification by anion-exchange resin (Bio-Rad AG MP-1). Purified Fe solutions were evaporated to dryness, refluxed three times in 0.5 mL HNO_3 to eliminate chlorides, and finally dissolved in 1% HNO_3 at 3 ppm for Thermo Neptune MC-ICP-MS analysis. Whole procedure Fe recoveries were 98%–101%, with blanks less than 0.3% of the total. Mass fractionation was calibrated using standard sample bracketing, and Fe isotope compositions are expressed as per mil deviations relative to the IRMM-014 standard:

$$\delta^{56}Fe_{(\text{‰})} = 1000 \times \left[\left(^{56}Fe/^{54}Fe_{sample} \right) / \left(^{56}Fe/^{54}Fe_{IRMM-014} \right) - 1 \right] \quad (1)$$

Repeated analyses of the in-house standard (CAGS Fe) exhibited consistent offsets relative to the IRMM-014 Fe isotope reference material, with a mean Fe isotope composition of $\delta^{56}Fe = 0.81 \pm 0.08$‰ (2 SD, $n = 8$), in agreement with previously reported values[71]. Reference materials BCR-2 and BIR-1 were analyzed to monitor instrumental accuracy, yielding $\delta^{56}Fe$ values of 0.10 ± 0.07‰ and 0.03 ± 0.08‰, respectively, which were also consistent with published results[72].

Whole rock $\delta^{56}Fe$ compositions reflect a mixture of detrital and authigenic signals. Here, we use a simple mixing model to calculate $\delta^{56}Fe$ values of Fe_{HR}: $\delta^{56}Fe = (Fe_{HR} \times \delta^{56}Fe_{HR} + Fe_U \times \delta^{56}Fe_U)/(Fe_{HR} + Fe_U)$, where $\delta^{56}Fe$ is the measured whole rock value, $\delta^{56}Fe_{HR}$ is the isotopic composition of highly reactive iron, and $\delta^{56}Fe_U$ is the isotopic composition of unreactive iron, which we assume to have crustal values (i.e., 0.1‰)[45].

Mo isotope analyses

Chemical procedures for Mo isotope analyses using a ^{97}Mo-^{100}Mo double spike follow those suggested by Li et al.[73] at the Guizhou Tongwei Analytical Technology Company Limited in Guizhou. Siliciclastic and Fe-Mn chemical sedimentary rocks were dissolved in ~3 mL of *aqua regia* at 120 °C for 12 h. Molybdenum separation and purification were achieved using N-benzoyl-N-phenyl hydroxylamine (BPHA) chromatographic resin[25]. The purified Mo sample solutions were used to determine Mo isotopic composition, using a Thermo-Fisher Scientific Neptune Plus multiple collector inductively coupled plasma mass spectrometer (MC-ICP-MS) at the State Key Laboratory of Isotope Geochemistry, Guangzhou Institute of Geochemistry. The isotopic compositions of Mo were reported as $\delta^{98/95}Mo$ (simplified as $\delta^{98}Mo$) relative to the NIST SRM 3134 (= 0.25‰) standard[74]:

$$\delta^{98/95}Mo_{(\text{‰})} = \left\{ \left[\left(^{98/95}Mo_{sample} \right) / \left(^{98/95}Mo_{NIST3134} \right) - 1 \right] \times 1000 \right\} + 0.25$$

(2)

The standard solution (NIST 3134) and two reference materials (AGV-2 and IAPSO) were measured repeatedly along with the samples, with $\delta^{98}Mo$ values of 0.25 ± 0.05‰ (2 SD, $n = 25$), -0.08 ± 0.02‰ (2 SD, $n = 3$) and 2.31 ± 0.01‰ (2 SD, $n = 5$) respectively, consistent with previously reported values[73]. The double spike calculation was accomplished using an in-house created Microsoft Virtual Basic program[75]. The Mo concentration of procedural blanks was 0.32 ± 0.06 ng (2 SD, $n = 3$), far lower than the total Mo content of samples.

Calculation of seawater Mo isotopic compositions from Mn-Fe oxide data

Calculating seawater $\delta^{98}Mo$ by the Mn-Fe oxides follows the suggestion from Goto et al.[35]. If the Mn-Fe oxides have high Mn content (Mn/Fe ratio > 10), Fe in samples likely does not affect the Mo isotope fractionation. Thus, the determination of the seawater $\delta^{98}Mo$ value could be done using a simple calculation with the measured $\delta^{98}Mo$ value plus the respective isotopic fractionations[35].

$$\delta^{98}Mo_{GSW} = \delta^{98}Mo_{sample} - \Delta_{Mn-SW} \quad (3)$$

where $\delta^{98}Mo_{GSW}$ represents Mo isotope composition of global seawater (GSW); Δ_{Mn-SW} is the isotope fractionation factor generated by the adsorption of dissolved seawater Mo to Mn oxides

When the oxides have Mn/Fe ratios between 1 and 10, both isotope fractionation and efficiency of Mo adsorption onto Mn and Fe oxides should be considered when calculating seawater $\delta^{98}Mo$[35].

$$\delta^{98}Mo_{GSW} = \frac{(f \times k + 1)\delta^{98}Mo_{sample} - f \times k \times \Delta_{Mn} - \Delta_{Fe}}{f \times k + 1} \quad (4)$$

where f is the Mn/Fe ratio of the oxides (wt%/wt%) and k is a ratio of Mo adsorption efficiency onto Mn oxides to Mo adsorption onto Fe oxides. The specific process of back-calculating $\delta^{98}Mo_{GSW}$ by Wafangzi Mn-Fe ores and related parameters is shown in Supplementary Information and Supplementary Data 2.

Molybdenum isotope mass balance model

A steady-state isotopic mass-balance model can be used to quantitatively evaluate the Mo isotopic composition of seawater[27–29]. Generally, a fixed riverine and ground water (River + GW) input of Mo is balanced by three major sinks[27]: (1) Oxygenated environments (O; $O_2 > 10\,\mu M$, representing a threshold value to support the Mn oxides precipitation and burial), and the main pathway for Mo precipitation is through adsorption onto Mn(IV) oxides[46,47,76]; (2) Strongly sulfidic environments (SE; bottom water $[H_2S]_{aq} > 11\,\mu M$), where Mo will be quantitatively removed from the water column[33,77–79]; and (3) Intermediate environments (M; bottom water redox states range between weakly oxygenated with dissolved oxygen $< 10\,\mu M$, to weakly sulfidic with $[H_2S]_{aq} < 11\,\mu M$), where Mo isotopic fractionation is mainly controlled by authigenic sulfide or organic matter, which most efficiently sequester Mo[80]. As the adsorption capacity of Fe(III) oxides is far less than sulfide minerals and organic matter, the Fe-oxides in intermediate environments may not be the main host phase that influences Mo isotope fractionation[49].

Assuming that the oceanic Mo cycling was steady, the fractions of the fluxes (f) can be expressed as:

$$f_{\text{River} + \text{GW}} = 1 = \sum f_i (i = O; M; SE) \tag{5}$$

Integration of modern parameters (e.g., input flux (F, $g \cdot yr^{-1}$), output burial rates (R, $g \cdot m^{-2} \cdot yr^{-1}$), seafloor areas ($A$, m^2), isotope fractionations (Δ); see Supplementary Data 2) yields the following equation:

$$\delta^{98}\text{Mo}_{\text{GSW}} - [\delta^{98}\text{Mo}_{\text{River} + \text{GW}} \times f_{\text{River} + \text{GW}}] = \sum f_i \times \delta_i \tag{6}$$

where $\delta^{98}\text{Mo}_{\text{GSW}}$ represents the Mo isotope composition of global seawater (GSW); $\delta_i = \delta^{98}\text{Mo}_{\text{GSW}} + \Delta_i$, $i = O; M; SE$.

The fractional flux under each setting can be described as:

$$f_i = A_i \times R_i / F_{\text{River} + \text{GW}} \tag{7}$$

Assuming that the Mo output rates (R, $g \cdot m^{-2} \cdot yr^{-1}$) of different settings at a given time have the same linear relationship with the corresponding modern values, the Mo output rate in the paleo-oceans can be represented as:

$$R_i = \varphi R_{i-\text{modern}}; \varphi \text{ is a constant}; i = O; M; SE \tag{8}$$

then

$$A_i = f_i \times F_{\text{River} + \text{GW}} / R_i, i = O; M; SE \tag{9}$$

Here the variables $R_{i\text{-modern}}$ and $F_{\text{River}+\text{GW}}$ can be readily canceled out when computing the area proportion of each setting:

$$AO : AM : ASE = \frac{f_O}{R_O} : \frac{f_M}{R_M} : \frac{f_{SE}}{R_{SE}} \tag{10}$$

The selection of parameters and sensitivity analysis are detailed in Supplementary Information and Supplementary Data 2.

Data availability

All data supporting the findings of this study have been deposited in the Zenodo database under accession code (https://doi.org/10.5281/zenodo.17218383).

References

1. Lyons, T. W. et al. Co-evolution of early environments and microbial life. *Nat. Rev. Microbiol.* **22**, 572–586 (2024).
2. Planavsky, N. J. et al. Low Mid-Proterozoic atmospheric oxygen levels and the delayed rise of animals. *Science* **346**, 635–638 (2014).
3. Cole, D. B. et al. A shale-hosted Cr isotope record of low atmospheric oxygen during the Proterozoic. *Geology* **44**, 555–558 (2016).
4. Planavsky, N. J. et al. Widespread iron-rich conditions in the mid-Proterozoic ocean. *Nature* **477**, 448–451 (2011).
5. Reinhard, C. T. et al. Proterozoic ocean redox and biogeochemical stasis. *Proc. Natl. Acad. Sci.* **110**, 5357–5362 (2013).
6. Alcott, L. J., Mills, B. J. W. & Poulton, S. M. Stepwise Earth oxygenation is an inherent property of global biogeochemical cycling. *Science* **366**, 1333–1337 (2019).
7. Gilleaudeau, G. J. et al. Molybdenum isotope and trace metal signals in an iron-rich Mesoproterozoic ocean: A snapshot from the Vindhyan Basin, India. *Precambrian Res.* **343**, 105718 (2020).
8. Wang, C. L. et al. Strong evidence for a weakly oxygenated ocean-atmosphere system during the Proterozoic. *Proc. Natl. Acad. Sci.* **119**, 1–8 (2022).
9. Poulton, S. W. & Canfield, D. E. Ferruginous conditions: a dominant feature of the ocean through Earth's history. *Elements* **7**, 107–112 (2011).
10. Poulton, S. W., Fralick, P. W. & Canfield, D. E. Spatial variability in oceanic redox structure 1.8 billion years ago. *Nat. Geosci.* **3**, 486 (2010).
11. Zhang, S. C. et al. Sufficient oxygen for animal respiration 1,400 million years ago. *Proc. Natl. Acad. Sci.* **113**, 1731–1736 (2016).
12. Canfield, D. E. et al. Petrographic carbon in ancient sediments constrains Proterozoic Era atmospheric oxygen levels. *Proc. Natl. Acad. Sci.* **118**, e2101544118 (2021).
13. Chen, G. X. et al. Reconstructing Earth's atmospheric oxygenation history using machine learning. *Nat. Commun.* **13**, 5862 (2022).
14. Zhang, S. C., Wang, H. J., Wang, X. M. & Ye, Y. T. The mesoproterozoic oxygenation event. *Sci. China Earth Sci.* **64**, 2043–2068 (2021).
15. Reinhard, C. T., Planavsky, N. J., Olson, S. L., Lyons, T. W. & Erwin, D. H. Earth's oxygen cycle and the evolution of animal life. *Proc. Natl. Acad. Sci.* **113**, 8933–8938 (2016).
16. Reinhard, C. T. & Planavsky, N. J. The history of ocean oxygenation. *Ann. Rev. Mar. Sci.* **14**, 331–353 (2022).
17. Pisarevsky, S. A., Elming, S. A., Pesonen, L. J. & Li, Z. X. Mesoproterozoic paleogeography: Supercontinent and beyond. *Precambrian Res.* **244**, 207–225 (2014).
18. Zhang, S. H. et al. A temporal and causal link between ca. 1380 Ma large igneous provinces and black shales: Implications for the Mesoproterozoic time scale and paleoenvironment: Implications for the Mesoproterozoic time scale and paleoenvironment. *Geology* **46**, 963–966 (2018).
19. Yang, S., Kendall, B., Lu, X. Z., Zhang, F. F. & Zheng, W. Uranium isotope compositions of mid-Proterozoic black shales: Evidence for an episode of increased ocean oxygenation at 1.36 Ga and evaluation of the effect of post-depositional hydrothermal fluid flow. *Precambrian Res.* **298**, 187–201 (2017).
20. Diamond, C. W., Planavsky, N. J., Wang, C. L. & Lyons, T. W. What the ~1.4 Ga Xiamaling Formation can and cannot tell us about the mid-Proterozoic ocean. *Geobiology* **16**, 219–236 (2018).
21. Zhang, S. C. et al. Paleoenvironmental proxies and what the Xiamaling Formation tells us about the mid-Proterozoic ocean. *Geobiology* **17**, 225–246 (2019).
22. Heard, A. W. et al. Coupled vanadium and thallium isotope constraints on Mesoproterozoic ocean oxygenation around 1.38-1.39 Ga. *Earth Planet. Sci. Lett.* **610**, 118127 (2023).

23. Sheen, A. I. et al. A model for the oceanic mass balance of rhenium and implications for the extent of Proterozoic ocean anoxia. *Geochim. Cosmochim. Acta* **227**, 75–95 (2018).

24. Hardisty, D. S. et al. Perspectives on Proterozoic surface ocean redox from iodine contents in ancient and recent carbonate. *Earth Planet. Sci. Lett.* **463**, 159–170 (2017).

25. Diamond, C. W. & Lyons, T. W. Mid-Proterozoic redox evolution and the possibility of transient oxygenation events. *Emerg. Top. Life Sci.* **2**, 235–245 (2018).

26. Yang, H. Y. et al. 1.44 Ga Oxygenation Event: Evidence From the Southern Margin of North China. *J. Geophys. Res.: Biogeosci.* **129**, e2023JG007787 (2024).

27. Kendall, B., Dahl, T. W. & Anbar, A. D. The stable isotope geochemistry of molybdenum. *Rev. Mineral. Geochem.* **82**, 683–732 (2017).

28. Qin, Z. et al. Molybdenum isotope-based redox deviation driven by continental margin euxinia during the early Cambrian. *Geochim. Cosmochim. Acta* **325**, 152–169 (2022).

29. Xu, D. T. et al. Extensive sea-floor oxygenation during the early Mesoproterozoic. *Geochim. Cosmochim. Acta* **354**, 186–196 (2023).

30. Miller, C. A., Peucker-Ehrenbrink, B., Walker, B. D. & Marcantonio, F. Re-assessing the surface cycling of molybdenum and rhenium. *Geochim. Cosmochim. Acta* **75**, 7146–7179 (2011).

31. Kendall, B. et al. Recent advances in geochemical paleo-oxybarometers. *Annu. Rev. Earth Planet. Sci.* **49**, 399–433 (2021).

32. Kendall, B. & Ostrander, C. M. Oxygenation of the Proterozoic Earth's surface: An evolving story. In: Anbar A. D., Weis D. (Eds.), Treatise on Geochemistry, 3rd Edition v. 5, p. 297–336. Elsevier (2025).

33. Nägler, T. F. et al. Molybdenum isotope fractionation in pelagic euxinia: Evidence from the modern Black and Baltic Seas. *Chem. Geol.* **289**, 1–11 (2011).

34. Planavsky, N. J. et al. Evidence for oxygenic photosynthesis half a billion years before the Great Oxidation Event. *Nat. Geosci.* **7**, 283–286 (2014).

35. Goto, K. T. et al. A framework for understanding Mo isotope records of Archean and Paleoproterozoic Fe- and Mn-rich sedimentary rocks: Insights from modern marine hydrothermal Fe-Mn oxides. *Geochim. Cosmochim. Acta* **280**, 221–236 (2020).

36. Goto, K. T. et al. Progressive ocean oxygenation at ~2.2 Ga inferred from geochemistry and molybdenum isotopes of the Nsuta Mn deposit. *Ghana. Chem. Geol.* **567**, 120116 (2021).

37. Spinks, S. C. et al. Mesoproterozoic surface oxygenation accompanied major sedimentary manganese deposition at 1.4 and 1.1 Ga. *Geobiology* **21**, 28–43 (2023).

38. Yan, H. et al. Mineralogy of the 1.45 Ga Wafangzi manganese deposit in North China: Implications for pulsed Mesoproterozoic oxygenation events. *Am. Mineral.* **109**, 764–784 (2024).

39. Su, W. B. et al. SHRIMP U-Pb dating for a K-bentonite bed in the Tieling Formation, North China. *Chin. Sci. Bull.* **55**, 3312–3323 (2010).

40. Lyu, D. et al. Using cyclostratigraphic evidence to define the unconformity caused by the Mesoproterozoic Qinyu Uplift in the North China Craton. *J. Asian Earth Sci.* **206**, 104608 (2021).

41. Mei, M. X., Yang, F. J., Gao, J. H. & Meng, Q. F. Glauconites formed in the high-energy shallow-marine environment of the Late Mesoproterozoic: case study from Tieling Formation at Jixian Section in Tianjin, North China. *Earth Sci. Front.* **15**, 146–158 (2008).

42. Czaja, A. D. et al. Biological Fe oxidation controlled deposition of banded iron formation in the ca. 3770 Ma Isua Supracrustal Belt (West Greenland). *Earth Planet. Sci. Lett.* **363**, 192–203 (2013).

43. Busigny, V. et al. Iron isotopes in an Archean ocean analogue. *Geochim. Cosmochim. Acta* **133**, 443–462 (2014).

44. Johnson, C. M., Beard, B. L., Klein, C., Beukes, N. J. & Roden, E. E. Iron isotopes constrain biologic and abiologic processes in banded iron formation genesis. *Geochim. Cosmochim. Acta* **72**, 151–169 (2008).

45. Planavsky, N. J. et al. Iron isotope composition of some Archean and Proterozoic iron formations. *Geochim. Cosmochim. Acta* **80**, 158–169 (2012).

46. Barling, J. & Anbar, A. D. Molybdenum isotope fractionation during adsorption by manganese oxides. *Earth Planet. Sci. Lett.* **217**, 315–329 (2004).

47. Wasylenki, L. E., Rolfe, B. A., Weeks, C. L., Spiro, T. G. & Anbar, A. D. Experimental investigation of the effects of temperature and ionic strength on Mo isotope fractionation during adsorption to manganese oxides. *Geochim. Cosmochim. Acta* **72**, 5997–6005 (2008).

48. Goldberg, T., Archer, C., Vance, D. & Poulton, S. W. Mo isotope fractionation during adsorption to Fe (oxyhydr)oxides. *Geochim. Cosmochim. Acta* **73**, 6502–6516 (2009).

49. Scott, C. & Lyons, T. W. Contrasting molybdenum cycling and isotopic properties in euxinic versus non-euxinic sediments and sedimentary rocks: Refining the paleoproxies. *Chem. Geol.* **324-325**, 19–27 (2012).

50. McLennan, S. M. Relationships between the trace element composition of sedimentary rocks and upper continental crust. *Geochem. Geophys. Geosyst.* **2**, 4 (2001).

51. Kurzweil, F., Wille, M., Gantert, N., Beukes, N. J. & Schoenberg, R. Manganese oxide shuttling in pre-GOE oceans - evidence from molybdenum and iron isotopes. *Earth Planet. Sci. Lett.* **452**, 69–78 (2016).

52. Ye, Y. T. et al. Black shale Mo isotope record reveals dynamic ocean redox during the Mesoproterozoic Era. *Geochem. Perspect. Lett.* **18**, 16–21 (2021).

53. Kendall, B., Gordon, G. W., Poulton, S. W. & Anbar, A. D. Molybdenum isotope constraints on the extent of late Paleoproterozoic ocean euxinia. *Earth Planet. Sci. Lett.* **307**, 450–460 (2011).

54. Kendall, B., Creaser, R. A., Gordon, G. W. & Anbar, A. D. Re-Os and Mo isotope systematics of black shales from the Middle Proterozoic Velkerri and Wollogorang Formations, McArthur Basin, northern Australia. *Geochim. Cosmochim. Acta* **73**, 2534–2558 (2009).

55. Partin, C. A. et al. Largescale fluctuations in Precambrian atmospheric and oceanic oxygen levels from the record of U in shales. *Earth Planet. Sci. Lett.* **369-370**, 284–293 (2013).

56. Anbar, A. D. Oceans: Elements and evolution. *Science* **322**, 1481–1483 (2008).

57. Robbins, L. J. et al. Manganese oxides, Earth surface oxygenation, and the rise of oxygenic photosynthesis. *Earth Sci. Rev.* **239**, 104368 (2023).

58. Wei, W. et al. A transient swing to higher oxygen levels in the atmosphere and oceans at ~1.4 Ga. *Precambrian Res* **354**, 106058 (2021).

59. Xu, L. et al. Large igneous province emplacement triggered an oxygenation event at ~1.4 Ga: Evidence from Mercury and paleoproductivity proxies. *Geophys. Res. Lett.* **51**, e2023GL106654 (2024).

60. Zhang, S. C. et al. Subaerial volcanism broke mid-Proterozoic environmental stasis. *Sci. Adv.* **10**, eadk5991 (2024).

61. Luo, A. B., Sun, G. Y., Grasby, S. E. & Yin, R. S. Large igneous provinces played a major role in oceanic oxygenation events during the mid-Proterozoic. *Commun. Earth Environ.* **5**, 609 (2024).

62. Canfield, D. E. et al. A Mesoproterozoic iron formation. *Proc. Natl. Acad. Sci.* **115**, E3895–E3904 (2018).

63. Fang, H. et al. Manganese-rich deposits in the Mesoproterozoic Gaoyuzhuang Formation (ca. 1.58 Ga), North China Platform: Genesis and paleoenvironmental implications. *Palaeogeogr. Palaeoclimatol. Palaeoecol.* **559**, 109966 (2020).

64. Ernst, R. E. et al. Long-lived connection between southern Siberia and northern Laurentia in the Proterozoic. *Nat. Geosci.* **9**, 464 (2016).

65. Roberts, N. M. The boring billion? Lid tectonics, continental growth and environmental change associated with the Columbia supercontinent. *Geosci. Front.* **4**, 681–691 (2013).

66. Evans, D. A. & Mitchell, R. N. Assembly and breakup of the core of Paleoproterozoic-Mesoproterozoic supercontinent Nuna. *Geology* **39**, 443–446 (2011).

67. Shang, M. H. et al. A pulse of oxygen increase in the early Mesoproterozoic ocean at ca. 1.57-1.56 Ga. *Earth Planet. Sci. Lett.* **527**, 115797 (2019).

68. Poulton, S. W. & Canfield, D. E. Development of a sequential extraction procedure for iron: implications for iron partitioning in continentally derived particulates. *Chem. Geol.* **214**, 209–221 (2005).

69. Canfield, D. E., Raiswell, R., Westrich, J. T., Reaves, C. M. & Berner, R. A. The use of chromium reduction in the analysis of reduced inorganic sulfur in sediments and shales. *Chem. Geol.* **54**, 149–155 (1986).

70. Hou, K. J., Ma, X. D., Li, Y. H., Liu, F. & Han, D. Chronology, geochemical, Si and Fe isotopic constraints on the origin of Huoqiu banded iron formation (BIF), southeastern margin of the North China craton. *Precambrian Res.* **298**, 351–364 (2017).

71. Zhu, X. K. et al. High-precision measurements of Fe isotopes using MCICP-MS and Fe isotope compositions of geological reference materials. *Acta Petrologica et. Min.* **27**, 263–272 (2008).

72. Craddock, R. & Dauphas, N. Iron isotopic compositions of geological reference materials and chondrites. *Geostand. Geoanal. Res.* **35**, 101–123 (2010).

73. Li, J. et al. Measurement of the isotopic composition of molybdenum in geological samples by MC-ICP-MS using a novel chromatographic extraction technique. *Geostand. Geoanal. Res.* **38**, 345–354 (2013).

74. Nägler, T. F. et al. Proposal for an international molybdenum isotope measurement standard and data representation. *Geostand. Geoanal. Res.* **38**, 149–151 (2014).

75. Zhang, L., Li, J., Xu, Y. G. & Ren, Z. Y. The influence of the double spike proportion effect on stable isotope (Zn, Mo, Cd, and Sn) measurements by multicollector inductively coupled plasma-mass spectrometry (MC-ICP-MS). *J. Anal. Spectrom.* **33**, 555–562 (2018).

76. Tostevin, R. et al. Low-oxygen waters limited habitable space for early animals. *Nat. Commun.* **7**, 12818 (2016).

77. Erickson, B. E. & Helz, G. R. Molybdenum(VI) speciation in sulfidic waters. *Geochim. Cosmochim. Acta* **64**, 1149–1158 (2000).

78. Neubert, N., Nägler, T. F. & Böttcher, M. E. Sulfidity controls molybdenum isotope fractionation into euxinic sediments: Evidence from the modern Black Sea. *Geology* **36**, 775–778 (2008).

79. Bura-Nakic, E. et al. Coupled Mo-U abundances and isotopes in a small marine euxinic basin: Constraints on processes in euxinic basins. *Geochim. Cosmochim. Acta* **222**, 212–229 (2018).

80. Poulson, R. L. et al. Authigenic molybdenum isotope signatures in marine sediments. *Geology* **34**, 617–620 (2006).

81. Siebert, C., Nägler, T. F., von Blanckenburg, F. & Kramers, J. D. Molybdenum isotope records as a potential new proxy for paleoceanography. *Earth Planet. Sci. Lett.* **211**, 159–171 (2003).

82. Bekker, A. et al. Iron formations: their origins and implications for ancient seawater chemistry. In: Holland H. D., Turekian K. K. (Eds.), Treatise of Geochemistry, p. 561-628. Elsevier (2014).

83. Gilleaudeau, G. J. et al. Uranium isotope evidence for limited euxinia in mid-Proterozoic oceans. *Earth Planet. Sci. Lett.* **521**, 150–157 (2019).

84. Canfield, D. E. et al. Highly fractionated chromium isotopes in Mesoproterozoic-aged shales and atmospheric oxygen. *Nat. Commun.* **9**, 2871 (2018).

85. Gilleaudeau, G. J. et al. Oxygenation of the mid-Proterozoic atmosphere: Clues from chromium isotopes in carbonates. *Geochem. Perspect. Lett.* **2**, 178–187 (2016).

Acknowledgements

Author contributions

H.Y. and L.-G.X. collected samples in the field; H.Y., Z.Q., L.-G.X., J.-W.M., L.J.R., and K.O.K. designed this study; J.L. carried out Mo isotopes analysis; Z.Q. and B.K. performed the Mo mass balance model; H.Y. wrote the original version of the manuscript; L.-G.X., X.-Q.Y., D.-J.T.,. and Q.H. participated in the interpretation of the data; L.-G.X., J.-W.M., D.-J.T., Z.-Q.L., L.L., L.J.R., and B.K. D.E.C. and K.O.K. participated in the discussion and editing of the manuscript.

Competing interests

The authors declare no competing interests.

Additional information

Supplementary information The online version contains supplementary material available at https://doi.org/10.1038/s41467-025-65551-z.

Correspondence and requests for materials should be addressed to Lingang Xu or Jingwen Mao.

Peer review information *Nature Communications* thanks Edel Mary O'Sullivan and the other anonymous reviewer(s) for their contribution to the peer review of this work. A peer review file is available.

Reprints and permissions information is available at http://www.nature.com/reprints